J Mater Sci

The Physics of Metal Plasticity: in honor of Professor Hussein Zbib

Modeling dislocation interactions with grain boundaries in lath martensitic steels

Ossama Abou Ali Modad[1] and Mutasem A. Shehadeh[2,3,*]

[1] *Department of Industrial and Manufacturing Systems Engineering, University of Michigan, Dearborn, USA*
[2] *Department of Mechanical Engineering, Alfaisal University, Riyadh, Saudi Arabia*
[3] *Mechanical Engineering Department, American University of Beirut, Beirut, Lebanon*

Received: 30 August 2023
Accepted: 24 October 2023

ABSTRACT

Martensitic steels are widely used as a structural material in critical components of fossil fuel and nuclear power plants, such as boilers, pipes, and fittings. Martensitic steels are known to have a hierarchical microstructure that follows the Kurdjumov–Sachs (K–S) orientation relationship, where a prior austenite grain is composed of packets separated by high angle grain boundaries or packet boundaries, which are, in turn, divided into blocks or variants segregated by high angle grain boundaries called block boundaries. Blocks themselves are an agglomeration of laths divided by low angle grain boundaries named lath boundaries which have precipitates scattered on them. This work seeks to examine, using a couple dislocation dynamics—continuum mechanics approach called multiscale dislocation dynamics plasticity (MDDP), the interactions between dislocations and packet, block, lath boundaries, and precipitates under uniaxial tension loading and their effect on the mechanical response of the material. The simulations are conducted at a strain rate of 10^5 s^{-1} at room temperature. The main crystallographic features that arise during the deformation process were extracted and analyzed in terms of their contribution to the mechanical response of the material. The orientation relationship governing the microstructure of martensitic steels, namely, the K–S orientation relationship, was incorporated in MDDP in an effort to accurately capture the deformation behavior of the material in question. The strength of lath martensitic steel was analyzed as a function of the lath width, block size, and packet size to determine the appropriate effective grain size.

Handling Editor: M. Grant Norton.

Address correspondence to E-mail: mshehadeh@alfaisal.edu

https://doi.org/10.1007/s10853-023-09084-0
Published online: 17 December 2023

Introduction

When the austenite (γ) phase with a face-centered cubic (FCC) crystal structure in steels is rapidly quenched to a low temperature, a diffusionless transformation forms a new phase with body-centered cubic (BCC) crystal structure. The transformation and the resulting phase are called the martensitic transformation and martensite (α'), respectively [54]. The morphology and crystallographic orientation relationship between prior austenite grains and the transformed martensite blocks depend on alloy composition [33]. Lath martensite forms in low carbon steels with a carbon content less than 0.6% with habit planes close to $\{111\}_{\gamma}$ [37]. A number of lath martensite steels have been reported to follow the Kurdjumow–Sachs (K–S) orientation relationship [27]. It has been shown that Ni also affects the martensite morphology where Fe–28.5%Ni steel forms plate martensite and has been shown to satisfy the Nishiyama–Wassermann (N–W) orientation relationship [24]. Martensitic steels have a hierarchical microstructure composed of prior austenite grains (PAGs) containing packets, blocks, and laths. Packet and block boundaries (high angle grain boundaries) separate the many misoriented packets and blocks [23]. These interfaces contribute to the superior mechanical properties of martensitic steels by obstructing dislocation motion at high angle grain boundaries [26, 36], which makes them an attractive choice for next-generation nuclear power plants [5, 50, 58]. In order to meet the safety requirements and the efficiency needs, predictive tools are required to assess the structural integrity of critical power plant components. Recent advances in multiscale material modeling provide a predictive capability to rigorously scrutinize the material response under a wide range of conditions. Such techniques also provide an explicit representation of the material microstructure and its effect on the overall performance under working conditions. The influence of microstructural features on the response of tempered martensitic steels must be properly quantified and detailed to design optimal materials and to properly assess the structural integrity of critical power plant components. A study using a finite element (FE) crystal plasticity model, where a representative volume element (RVE) that accounts for the microstructure of the material is taken from electron backscatter diffraction (EBSD) measurements [15], examined the deformation characteristics of a high chromium power plant steel at elevated temperatures and found good agreement with the experimental data, thus concluding that periodic boundary conditions can be used to represent the martensitic microstructure. Another approach at capturing the hierarchical packet–block–lath microstructure carried out by [52], involved the use of the Voronoi tessellation method where a volume/area is partitioned into different polygonal regions representing equiaxed grains with random crystal orientation distribution. Building on the work of [52], the microstructural deformation of an ex-service 9Cr–1 Mo tempered martensitic steel has been scrutinized by [34] through the use of EBSD and multiscale crystal plasticity modeling techniques, and the experimental and simulated deformation of a notched tension loaded specimen from the macroscale specimen level down to the block level are compared. A strain gradient crystal plasticity model incorporating statistically stored dislocations (SSDs) and geometrically necessary dislocations (GNDs) used by [51], investigated the effect of SSDs, GNDs on the yield and flow strengths of a martensitic P91 steel, the influence of the relevant microstructural length scales (PAG/packet/block diameter) on the global and local mechanical response has also been studied. Crystallographic and experimental studies carried out on multilayered steels consisting of two hard martensitic layers and a ductile layer of austenite were used to examine the correlation between slip system activation and the change in microstructure of lath martensitic steel [39]. Nanoindentation and micropillar compression tests were carried out on martensite and austenite phases in a 0.15 wt%C dual-phase sheet steel along with macroscopic uniaxial tensile tests on specimens of the same steel, the microstructures of the deformed micropillars were analyzed via TEM [14], the mechanical data obtained from the tensile tests along with the microstructural evolution were used to examine the deformation response of the steel in question. Due to the hierarchical microstructure of lath martensitic steels, different length scales are involved; therefore, understanding the size effects of each hierarchy, namely, packets, blocks, laths, and precipitates, is of paramount importance. [38] investigated the effect of block size in lath martensitic steel using TEM observations along with a Hall–Petch type analysis when analyzing the relationship between strength and structure. [30] found that the yield strength decreased with increasing packet and block widths according to a Hall–Petch relationship. This is further confirmed by [51] who used a strain gradient crystal plasticity

model using the Voronoi tessellation method to model the PAG/packet/block hierarchy and the effect of this hierarchy on the macro- and micro-scale mechanical behavior. Others [8, 32, 47] have used experimental methods to study and to determine the relevant structural parameters when analyzing the microstructure of lath martensitic steels. To the authors' best knowledge, the microstructure of lath martensitic steels has not been analyzed using 3D discrete dislocation dynamics (DDD). Due to the many length scales involved in lath martensitic microstructures and the presence of many grain boundaries (packet and grain boundaries), understanding the behavior at the microscale in response to a stimulus is essential for understanding the macroscale response. The interaction between dislocations and grain boundaries using 3D DDD has been extensively studied [12, 21, 31]. Specifically related to this work is the study conducted by [56] where a dislocation—GB interaction model is developed that considers both dislocation absorption and dislocation emission at the GBs. The premise of this model is that the framework used allows to model various types of GBs; however, they are not represented explicitly. To that end, this study aims to model the microstructure of a lath martensitic steel starting at the lath level up to the packet–block hierarchy steel by taking into account the K–S crystallographic orientation relationship using a multiscale FE–DDD methodology developed by [55]. Furthermore, the interactions of dislocations with block and lath boundaries and the influence of the lath width and the lath boundaries on the mechanical response of the material will be examined. This paper is detailed as follows. "Methodology" section details the methodology and the framework used to conduct the analysis. "Simulation setup" section presents the simulation setup for the considered scenarios. The results are laid out and discussed in "Lath boundaries, Packet–block simulations, and Size effects" sections, where the lath, packet–block structures, and the size effects are modeled and investigated, and finally, "Summary" section summarizes the findings of this study.

Methodology

MDDP

MDDP [55] is a simulation model that couples 3D discrete dislocation dynamics (DDD) with continuum finite element (FE) analysis. This coupling results in a hybrid elasto-viscoplastic framework to simulate plasticity in crystalline materials.

In DDD, plastic deformation is determined by the explicit evaluation of dislocations motion and interactions with each other as well as with other defects. Dislocation lines and curves are discretized into small segments of mixed character. The dynamics of the dislocation segments follows a Newtonian equation of motion. As the dislocation moves, it has to overcome local barriers such as the Peierls barrier (lattice friction) and the internal drag force. Additionally, the dislocation may encounter obstacles such as point defects and precipitates. Moreover, dislocation interactions with boundaries are incorporated where image stress of free and rigid boundaries are considered. In summary, the net driving force acting of any dislocation segment is given by the Peach–Kohler force F_i equation below such that;

$$F_i = F_{\text{Peierls}} + F_D + F_{\text{self}} + F_{\text{External}} + F_{\text{obstacle}} + F_{\text{image}} \tag{1}$$

where F_{Peierls} is the Peierls force arising from lattice friction, F_{external} is the force due to externally applied loads, F_D is the dislocation–dislocation interaction force, F_{self} is the dislocation self-force, F_{obstacle} is the dislocation–obstacle interaction force, and F_{image} is the image force from boundaries. Details on the evaluation of these forces provided in [55].

As mentioned above, the dynamics of dislocations is governed by a "Newtonian" equation of motion, consisting of an inertia term, viscous damping term, and driving force term such that,

$$m_i \dot{v}_{gi} + \frac{1}{M_i} v_{gi} = F_i \tag{2A}$$

where m_i is the effective dislocation segment mass, M_i is the dislocation mobility, and v_{gi} is the segment glide velocity. In BCC metals, it is established that the dislocation mobility is dependent not only on its glide velocity, but also on its character and the deformation temperature. These mobility features are incorporated in the DDD framework as discussed in [11, 45] such that

$$M_i = [M_{0\text{E}} + 99 \times M_{0\text{E}} \times \cos \alpha_i] \left(1 - \left(\frac{v_{gi}}{c_{\text{t}}}\right)^2\right) \frac{T_{\text{cr}}}{T} \tag{2B}$$

where T is the simulation temperature; v is the glide velocity; and α is the dislocation character that is the

angle between the dislocation line sense and its burger vector. T_{cr} is the critical temperature of the material which is the temperature above which the mobility of screw dislocation equalizes that of an edge dislocation (T_{cr} = 340 K for α-Fe); M_{0E} is the dislocation mobility of a pure edge segment at the reference temperature; and c_t is the material transverse speed of sound.

The equation of motion is then solved to find the velocities, and thus, the plastic strain rate $\dot{\varepsilon}_p$ and the plastic spin W_p are evaluated, respectively:

$$\dot{\varepsilon}^p = \sum_{i=1}^{N} \frac{l_i v_{gi}}{2V} \left(n_i \otimes b_i + b_i \otimes n_i \right) \tag{3}$$

$$W^p = \sum_{i=1}^{N} \frac{l_i v_{gi}}{2V} \left(n_i \otimes b_i - b_i \otimes n_i \right) \tag{4}$$

where l_i is the dislocation segment length, n_i is a unit normal to the slip plane, and V is the volume of the representative element. The above relations provide the most rigorous connection between the dislocation motion (the fundamental mechanism of plastic deformation in crystalline materials) and the macroscopic plastic strain, with its dependence on strength and applied stress being explicitly embedded in the calculation of the velocity of each dislocation.

In the macro-level, it is assumed that the material obeys the basic laws of continuum mechanics, *i.e.*, linear momentum balance and energy balance:

$$\operatorname{div} S = \rho \dot{v} \tag{5}$$

$$\rho C_v \dot{T} = \eta S \cdot \dot{\varepsilon}^p \tag{6}$$

In the above equations, S is the Cauchy stress tensor, T is the temperature, v_p is the particle velocity, and ρ, C_v, and K are mass density, specific heat, and thermal conductivity, respectively. For elasto-visco-plastic behavior, the strain rate tensor $\dot{\varepsilon}$ is decomposed into an elastic part $\dot{\varepsilon}_e$ and plastic part $\dot{\varepsilon}_p$ such that:

$$\dot{\varepsilon} = \dot{\varepsilon}^e + \dot{\varepsilon}^p \tag{7}$$

The elastic response is expressed using the incremental form of Hooke's law such that:

$$\overset{\circ}{S} = \left[C^e \right] \left[\dot{\varepsilon}^e \right] \tag{8}$$

where C^e is the anisotropic elastic stiffness tensor. Combining (6) and (7) leads to:

$$\overset{\circ}{S} = \left[C^e \right] \left[\dot{\varepsilon} - \dot{\varepsilon}^p \right] \tag{9}$$

To correct for the actual boundary conditions when coupling DD with FE, the principle of superposition is applied. The dislocations contained within the RVE produce an internal stress, and the effective total stress within the RVE is the sum of all internal stresses and any externally applied stress. Thus, the long-range stresses are treated as internal variables which leads to an efficient numerical scheme. With this approach, complex dislocation structures with mixed boundary conditions are easily dealt with. Details of the MDDP framework can be found in [40], Shehadeh * et al., 2005; [43, 44, 55].

Geometry, material parameters, and boundary conditions

To model the behavior of martensitic steels, a Burgers vector of $b = 2.48$ Å is used. A shear modulus of $G = 78$ GPa is adopted with a Poisson's ratio of 0.34. A discretization length of 50 b is used. The ambient mobility of a pure edge dislocation is set as $M_{0E} = 10^3$ Pa^{-1}s^{-1} whereas the screw dislocation mobility is amplified by a factor of 100 so as to mimic the behavior of a real BCC crystal, that is, $M_{0S} = 10^5$ Pa^{-1}s^{-1} [9, 10, 16, 17, 45]. A mass density of 7800 kg/m^3 is used. Boundary conditions are divided into FE boundary conditions and DD boundary conditions. In DD, all surfaces of the RVE are subjected to periodic boundary conditions which are used to model dislocation motion and interaction in bulk crystals, that is, when a dislocation segment leaves a surface, it emerges from the opposite side of the RVE. In FE, the loading of the samples is designed to mimic a constant strain rate uniaxial tension condition. A displacement was applied on the upper surface so that a constant velocity over the entire simulation duration is attained. The side surfaces are kept free while the bottom surface is fixed. The resulting strain rate of this loading was found to be 10^5 s^{-1}.

Lath boundaries

For the lath simulations, the area of interest in the martensitic microstructure is the laths within a certain block. Two low angle tilt boundaries are constructed for the MDDP simulations in order to simulate a lath substructure. The boundaries used are based on the pure tilt boundary described by [22]. The boundary

width is equal to the RVE width in both the x and y directions. The reference frame has been rotated as shown in Fig. 1 so that the dislocation lines are parallel to the x-axis, and the Burgers vector is oriented so as to obtain pure edge dislocations. The GB configuration and the boundary conditions are shown below where L_x and L_y are fixed to 2 μm, and L_z is twice the lath width D in order to maintain periodicity. $\frac{1}{2}\left[\bar{1}1\bar{1}\right]$ dislocations on a (110) slip plane are piled up to form the GB. The separation distance between dislocation lines within the GB is $d = 71.5$ nm. The misorientation angle θ is calculated by using of Frank's formula, such that $\theta = b/d$ yielding a tilt angle of 0.23°. The LAGB model used in this paper is that of a perfect pure edge tilt boundary as shown below.

Kurdjumow–Sachs orientation relationship implementation

The transformation mechanism from austenite to martensite in the K–S relationship is based on shear and rotation. The K–S orientation relationship is an expression of the martensitic transformation from austenite (γ) to martensite (α') and is written as follows:

$$\{111\}_\gamma // \{110\}_{\alpha'},\ <110>_\gamma // <111>_{\alpha'}.$$

The $\{111\}_\gamma$ and $\{110\}_{\alpha'}$ correspond to the close packed slip planes of the austenite and martensite phases, respectively. Due to symmetry, cubic systems have 24 equivalent crystallographic variants in martensite which evolve from a single grain of austenite if the K–S orientation relationship is maintained. That is, 24 combinations of planes/directions satisfy the K–S relationship. The crystallographic variants V_1, V_2, … V_{24} are listed in Table 3.

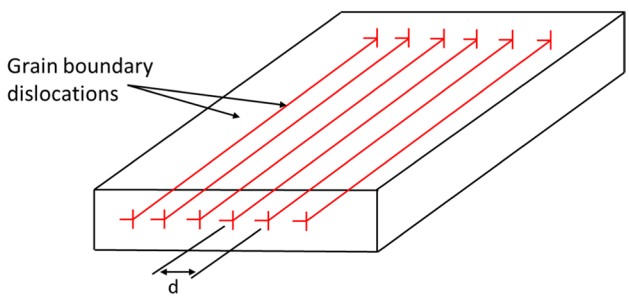

Figure 1 LAGB schematic representation.

The change in crystallographic orientation from austenite to martensite is expressed by a matrix equation:

$$\boldsymbol{M} = \boldsymbol{TA}, \tag{10}$$

where $\boldsymbol{T}$ is the orientation transformation matrix, and $\boldsymbol{M}$ and $\boldsymbol{A}$ are the orientation matrices made up of three orthogonal unit vectors indicating the crystallographic directions for the martensite and austenite phases, respectively [23]. The misorientation angle between two different variants is calculated using the orientations for the 24 martensite variants ($\boldsymbol{M_i}$ where $i = 1, 2, \ldots 24$). The rotation matrix $\boldsymbol{R}$ between the $\boldsymbol{M}_1$ and $\boldsymbol{M}_2$ variants, for example, is calculated from the below equation:

$$\boldsymbol{M}_2 = \boldsymbol{R}\boldsymbol{M}_1. \tag{11}$$

According to Table 3, a maximum of six possible variants or blocks can appear in a single packet. Therefore, for this study, the RVE that will be used in this work is going to be divided in two as shown in Fig. 2 in order to represent a packet containing two martensite variants, namely, the $\boldsymbol{V}_1$ and $\boldsymbol{V}_2$ variants. The $\boldsymbol{M}_1$ orientation matrix for the $\boldsymbol{V}_1$ variant is chosen as $\boldsymbol{M}_1 = \begin{pmatrix} 1 & 0 & 0 \\ 0 & 1 & 0 \\ 0 & 0 & 1 \end{pmatrix}$. In order to acquire the orientation matrix for the $\boldsymbol{V}2$ variant, first, the rotation matrix $\boldsymbol{R}$ is calculated from [24] and was found to be $\boldsymbol{R} = \begin{pmatrix} -1/2 & 3/5 & -3/5 \\ -3/5 & 1/4 & 3/4 \\ 3/5 & 3/4 & 1/4 \end{pmatrix}$, therefore resulting in $\boldsymbol{M}_2 = \begin{pmatrix} -1/2 & 3/5 & -3/5 \\ -3/5 & 1/4 & 3/4 \\ 3/5 & 3/4 & 1/4 \end{pmatrix}$. The mismatch between $\boldsymbol{V}_1$ and $\boldsymbol{V}_2$ was calculated by using the dot product formula between the slip direction of $\boldsymbol{V}_1$, namely, $\vec{b_1} = [-0.577\ -0.577\ 0.577]$, and $\boldsymbol{V}_2$ which has now been rotated with respect to $\boldsymbol{V}_1$ to obtain a slip direction $\vec{b_2} = [-0.418\ 0.642\ 0.642]$. The mismatch was found to be 60° which conforms with the findings of [23] outlined in Table 4.

The packet and block boundaries depicted in Fig. 3 are modeled as frictional barriers with very high frictional stresses. Since packet and block boundaries are high angle grain boundaries (HAGBs), thus, impenetrable boundaries. To reflect that fact, a very high frictional force is applied on the locations of the packet and block boundaries. The surfaces of the

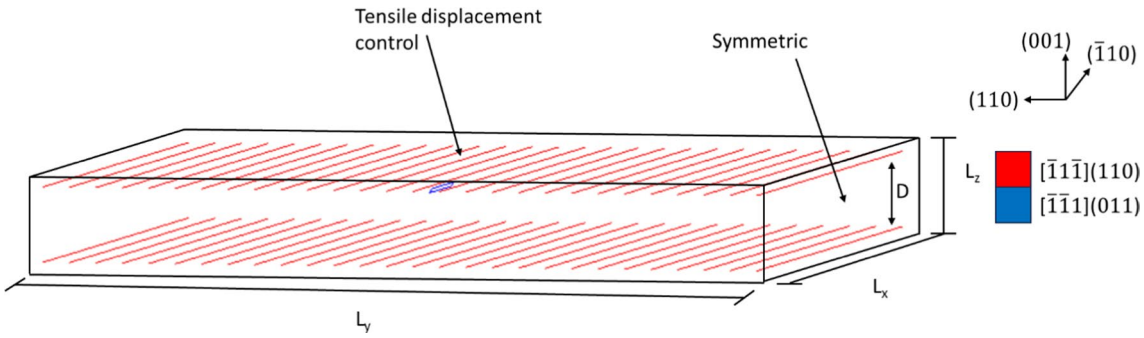

Figure 2 RVE schematic showing the simulation setup along with the boundary conditions. Shown here are two LAGBs separated by a distance $D = {}^{L_z}/_{2}$. A Frank–Read (FR) source is placed in the middle between both LAGBs and belongs to the $[\bar{1}1\bar{1}]$ (011) slip system (blue). The grain boundary dislocations belong to the $[\bar{1}1\bar{1}]$ (110) slip system (red).

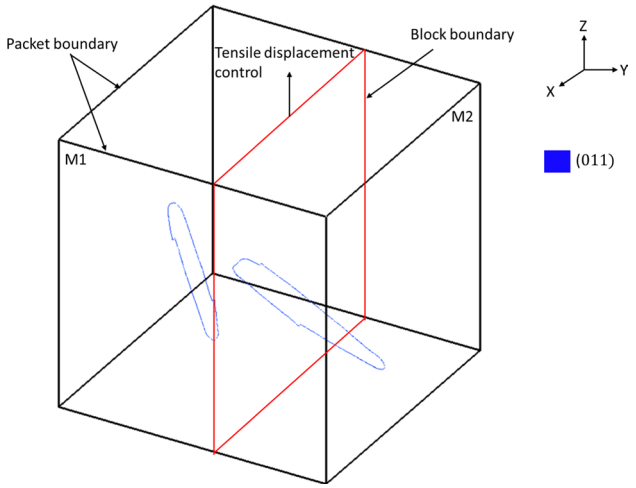

Figure 3 Simulation setup depicting a packet containing the $\boldsymbol{V}_1$ and $\boldsymbol{V}_2$ martensite variants with orientation $\boldsymbol{M}_1$ and $\boldsymbol{M}_2$, respectively. Each block contains a single FR source. Black and red lines represent packet and block boundaries, respectively. The block boundary serves to divide the packet into the two martensite variants. Packet and block boundaries are modeled as high frictional barriers. The 60° mismatch is showcased through the mismatch between the (011) FR sources.

RVE represent the packet boundaries while the block boundary (red plane shown in Fig. 3) is situated in the middle of the RVE dividing it into two blocks.

Simulation setup

Lath boundaries

In addition to the pure edge dislocation lines placed on the (110) $[\bar{1}1\bar{1}]$ slip system to simulate the LAGB, a single Frank–Read source is placed on the (011) $[\overline{1}\overline{1}1]$ slip system to act as a dislocation generation mechanism that can move via glide. The estimated initial dislocation density is $\rho_{\text{dis}} \approx 10^{13}\text{m}^{-2}$. The simulation setup is depicted in Fig. 1 with a lath width that varies from 0.2 to 0.5 μm. Table 1 summarizes the different sizes of the RVE, and the lath widths used in the simulations. The simulated samples are subjected to uniaxial tension at a strain rate of $10^5\ \text{s}^{-1}$.

Table 1 Summary of the lath simulation scenarios

Lath width ($\boldsymbol{D}$) (μm)	$\boldsymbol{L}_x$(μm)	$\boldsymbol{L}_y$(μm)	$\boldsymbol{L}_z$(μm)
0.2	2	2	0.4
0.3	2	2	0.6
0.4	2	2	0.8
0.5	2	2	1

Packet–block simulations

The next hierarchy that needs to be studied after the lath substructure is at the packet block level. Packets can contain up to six possible martensite variants. The scope of this work is limited to modeling two martensite variants within a single packet, namely, the $\boldsymbol{V}_1$ and $\boldsymbol{V}_2$ variants, Fig. 3 shows a schematic describing the simulation scenarios used to simulate the mechanical response at the packet–block level. Future work aims to expand the K–S relationship to include more than two variants. For that purpose, the RVE will be divided into two parts, the left part representing the $\boldsymbol{V}_1$ variant with $\boldsymbol{M}_1 = \begin{pmatrix} 1 & 0 & 0 \\ 0 & 1 & 0 \\ 0 & 0 & 1 \end{pmatrix}$

Table 2 Summary of the packet/block scenarios considered and their dimensions ($L_x \times L_y \times L_z$)

Packet size (μm^3)	Block size (μm^3)
$2 \times 2 \times 2$	$2 \times 1 \times 2$
$3 \times 3 \times 3$	$3 \times 1.5 \times 3$
$4 \times 4 \times 4$	$4 \times 2 \times 4$

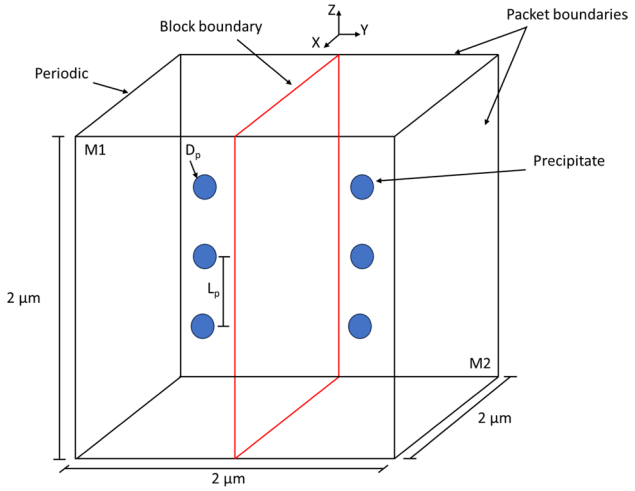

Figure 4 Dislocation–precipitate–boundary interaction simulation setup.

orientation matrix, and the right part of the RVE stands for the V_2 variant with the orientation matrix $M_2 = \begin{pmatrix} -1/2 & 3/5 & -3/5 \\ -3/5 & 1/4 & 3/4 \\ 3/5 & 3/4 & 1/4 \end{pmatrix}$. The orientation matrices were calculated in "Methodology" section, and the mismatch between V_1 and V_2 was found to be 60°.

The samples are subjected to uniaxial tension loading conditions at 10^5 s^{-1} strain rate and periodic boundary conditions. The initial dislocation density is $\rho \approx 10^{11} m^{-2}$. The effect of the initial dislocation density on the mechanical response is examined in "Lath boundaries" section. Table 2 details the sizes of the packets and blocks simulated. The packet and block sizes used in this paper are based on the findings of [51]. The dimension of interest for blocks is the smallest dimension, namely, L_y.

Finally, for completeness' sake, the precipitate is also modeled as a frictional sphere, similar to the way, packet and block boundaries are modeled, and their effect on the mechanical behavior and dislocation density, along with the dislocation interactions with the precipitate and boundaries, is investigated (Fig. 4).

Lath boundaries

Mechanical response

Figure 5 shows the stress and strain diagram for the simulated lath widths ranging between 0.2 and 0.5 μm at a constant strain rate of 10^5 s^{-1} at 300 K. Analyzing the stress–strain curves reveals the following about the material response:

1. Initially, the behavior is linear elastic overshoot ranging between 1100 and 1200 MPa, which is then followed by instantaneous stress relaxation.
2. Following the elastic overshoot and relaxation, plastic flow is initiated at ~ 700 MPa. Gradual strain hardening is observed up until ~ 2% strain is achieved. The plastic regime is characterized by a serrated curve as shown in Fig. 5b.
3. The mechanical behavior in the plastic regime does not exhibit any meaningful hardening. Harkening back to the study by [56], it is mentioned that the strain hardening rate and the flow stress of nanopillars containing a rigid GB are significantly higher than that in the case of a penetrable GB due to dislocation pile up. They determined that pillars with a penetrable GB can release stress concentration at the GB thus lowering the flow stress and weakening the hardening rate. In the context of the current lath boundaries investigation, given that the lath boundaries are modeled as penetrable LAGBs, the insignificant hardening exhibited by the mechanical behavior in Fig. 5 can be explained by the phenomenon observed by [56]. When the dislocation is first trapped by the GB, hardening takes place thus increasing the flow stress, then when it is released, the flow stress is lowered thus balancing the hardening and relaxation mechanisms at the GB.

Microstructure effect on the mechanical response

To gain a better understanding of the mechanical response, it is essential to analyze the role of the microstructure. For that reason, snapshots of the dislocation microstructure from the 0.2-μm lath width sample simulated at 10^5 s^{-1} strain rate at room temperature are shown in Fig. 6. Initially, two LAGBs are constructed by piling up pure edge dislocations on the (1 1 0) slip plane, and a single prismatic FR

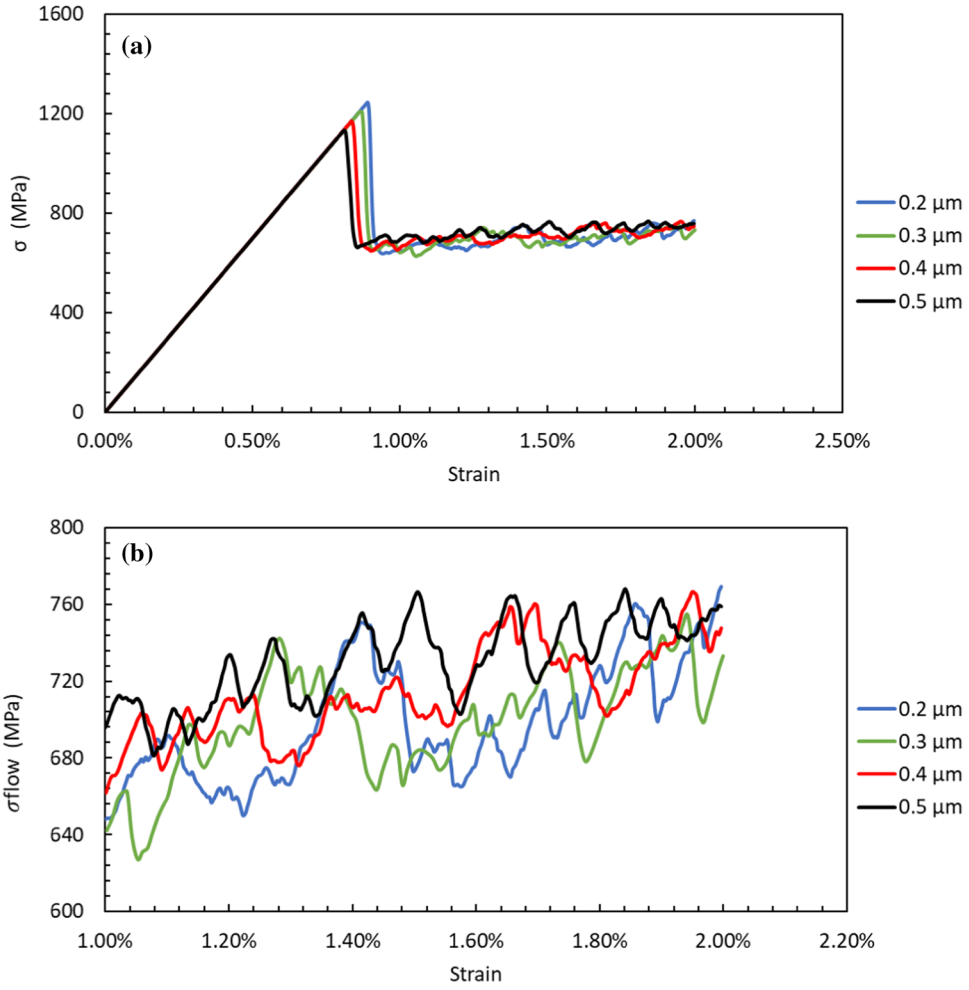

Figure 5 **a** Stress–strain diagram showing the material response to applied load. **b** Plastic regime of the material showing serrations in the stress–strain curves which are attributed to dislocation–GB interactions.

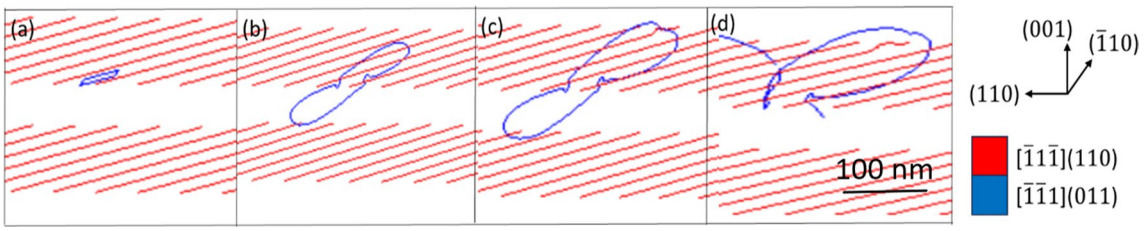

Figure 6 Snapshots of the GB–dislocation interaction. **a** Inactive prismatic FR source, the color red corresponds to the GB while the blue corresponds to the FR source and the subsequent generated dislocations. **b** FR sources start to bow out asymmetrically due to the difference in the lattice friction and mobility between edge and screw components. **c** As the stress increases, the first instance of dislocation—GB interaction takes place where the dislocation gets pinned on the GB (shown with arrow). **d** Once the yield stress is reached, the dislocation is unpinned and penetrates the boundary causing local plastic deformation in the form of a small step on the GB.

source is placed between the LAGBs and is situated on the (0 1 1) slip plane. As illustrated in Fig. 5b, once the critical resolved shear stress is attained, the dislocation source starts to asymmetrically bow out due to the difference in mobility between its edge and screw components. As the loading proceeds, the first instance of a dislocation—GB interaction is observed, where upon first contact, the LAGBs prevent dislocation motion through them as shown in Fig. 6c. When the dislocation first touches the GB, a small step on

the GB dislocation starts to form, and the dislocation is pinned at the boundary. As the stress increases further, the dislocation is released from its pinning point and penetrates the GB leaving behind a jog on the GB as illustrated in Fig. 6d and causing local plasticity at the lath boundaries. This process dislocation pinning–unpinning is repeated as dislocations multiply which results in the observed serrations in the stress–strain diagrams. In other words, after the first instance of dislocation—GB interaction and following dislocation multiplication, another dislocation will be pinned on the GB causing local plastic deformation in the form of a jog on the GB where there was contact between the incident dislocation and the lath boundary. As the loading continues, the flow stress increases and once it reaches a critical value, the dislocation is unpinned and continues its motion through the sample as shown in Fig. 7. When the dislocation is unpinned, the stress magnitude drops slightly and then continues its increase until another dislocation is unpinned which results in another drop in stress. This process is illustrated in Fig. 8 in relation to the mechanical response for the 0.2-μm lath width case.

Another interesting microstructural feature that has been detected is the rearrangement of dislocations into dipole configurations (see Fig. 9), a configuration which leads to material hardening. However, it is worth noting that some dipoles are not stable and disassociate as if they are unzipping as shown in Fig. 10. In the final microstructural configurations in Fig. 11, it can be seen that for smaller lath widths, the number of dipoles is significantly higher than the number of dipoles present in the 0.4-μm and 0.5-μm cases, where in the larger lath widths, pile ups are present. The larger number of dipoles in the 0.2-μm and 0.3-μm cases is attributed to the GBs acting as walls that confine the dislocation motion in between them. This restricts the number of possible interactions between dislocations and forces them to adopt more energetically favorable configurations and interactions, namely, dipole formation and dislocation annihilation as shown experimentally by [42]. In contrast with this, the 0.4-μm and 0.5-μm cases, the separation distances between GB dislocations are further apart from each other. Thus, reducing the effect of their opposing stress field on the mobile. By examining the final microstructure of the 0.4-μm and 0.5-μm scenarios, it can be seen that in addition to dipole formation, pile ups can be seen in the upper left corner of the RVE. A snapshot of the pile up in the 0.5-μm case is shown in Fig. 12. The pile up results in a compressive stress reaching up to 400 MPa.

Dislocation density evolution

The effect of the dislocation density over time is scrutinized by plotting the dislocation density history as shown in Fig. 13. It can be observed that the dislocation densities follow a logarithmic trend in the form of$\rho(t) = Alog(t) + B$, where ρ is the dislocation density, t is the time, A, and B are fitting constants. By comparing the dislocation densities of the 0.3-μm, 0.4-μm, and 0.5-μm lath width cases to the dislocation density of the smallest lath width scenario, namely, the 0.2-μm case, it is seen that as the lath width increases, the dislocation density decreases. In other words, the smallest lath width, the 0.2 μm will have the largest dislocation density, and as the lath width increases, the dislocation density will decrease until the 0.5-μm lath width scenario is reached where it will have the smallest dislocation density. This occurs because, as

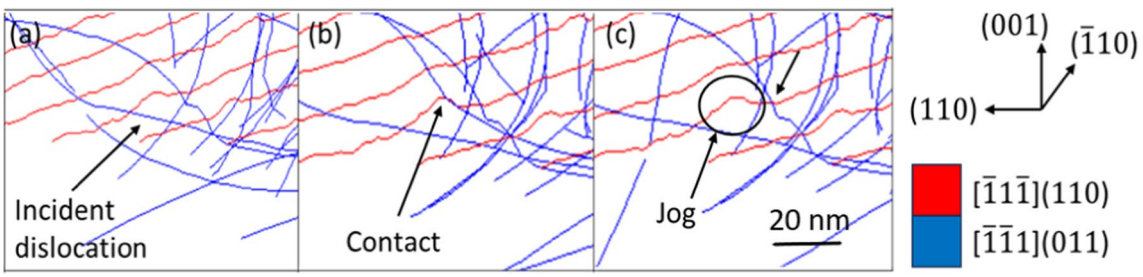

Figure 7 Snapshots of the dislocation pin/unpin process. **a** Incoming dislocation indicated by the arrow. **b** The dislocation is pinned on the GB causing a small step in the dislocation–GB. **c** Dislocation penetrates the GB and continues moving through the crystal (indicated by the arrow) thus increasing the size of the step on the GB (indicated by the circle).

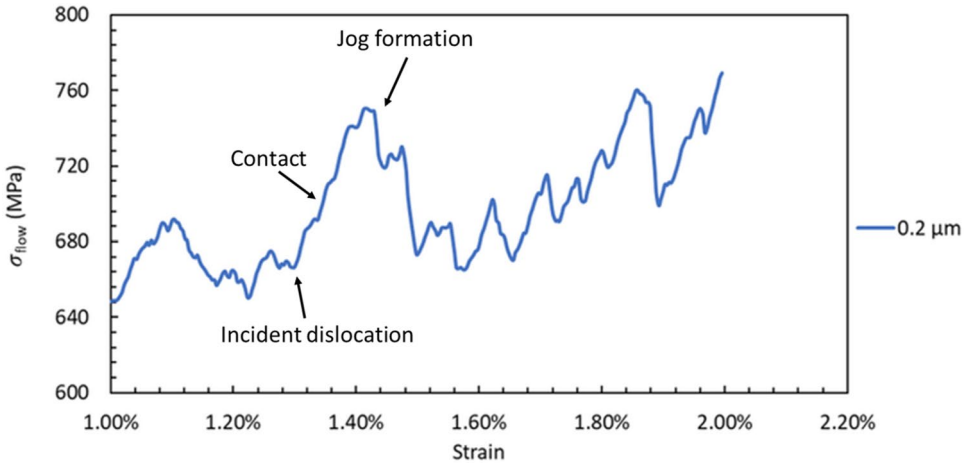

Figure 8 The pin/unpin mechanism shown on the stress-strain diagram. Once the incident dislocation approaches the lath boundary, a small jog starts to form and the flow stress starts to increase. When the dislocation makes contact with the GB it remains pinned at the GB and the flow stress continues to increase until it reaches a peak value of about 760 MPa. The dislocation then penetrates the G and leaves behind a permanent jog on the GB which results in relaxation. The jagged shape of the stress-strain diagram is indicative of this process being repeated throughout the loading process.

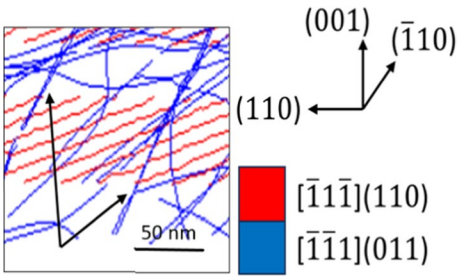

Figure 9 Dipole configuration (shown with arrows) which leads to hardening.

the lath width decreases, the volume of the sample will decrease and given the same number of dislocations at any given moment during the loading, there will be a higher dislocation density for the smaller volumes than the larger ones. It must be noted, however, that the dislocation density for all scenarios reaches a plateau once the slip systems have been activated. TEM observations by [42] show that dislocations in lath martensite tend to rearrange themselves into a stronger dipole character and that inside lath martensite, the dislocation density remains constant throughout the deformation process. Both of those findings are in support of the modeling results. In regard to the dipole formation, the smaller the lath width, the more dislocations tend to rearrange themselves into dipoles. The reason behind the plateau in the dislocation density curves is that the MDDP model assumes the LAGB to be ideal with very low misorientation angle; thus, the dislocations are easily able to penetrate the GB. However, the experimental findings of [42] which considered LAGBs with misorientation angles up to 5° still showed that the dislocation density inside laths remains constant during deformation, meaning that modeling the LAGB as ideal is

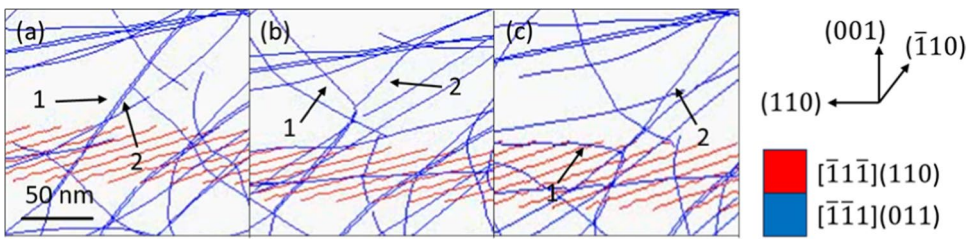

Figure 10 **a** Dislocations 1 and 2 in a dipole configuration. **b** Dislocation 1 starts to break away from dislocation 2 in an unzipping manner. **c** Dipole is disassociated, and individual dislocations continue gliding through the crystal to form more dipoles.

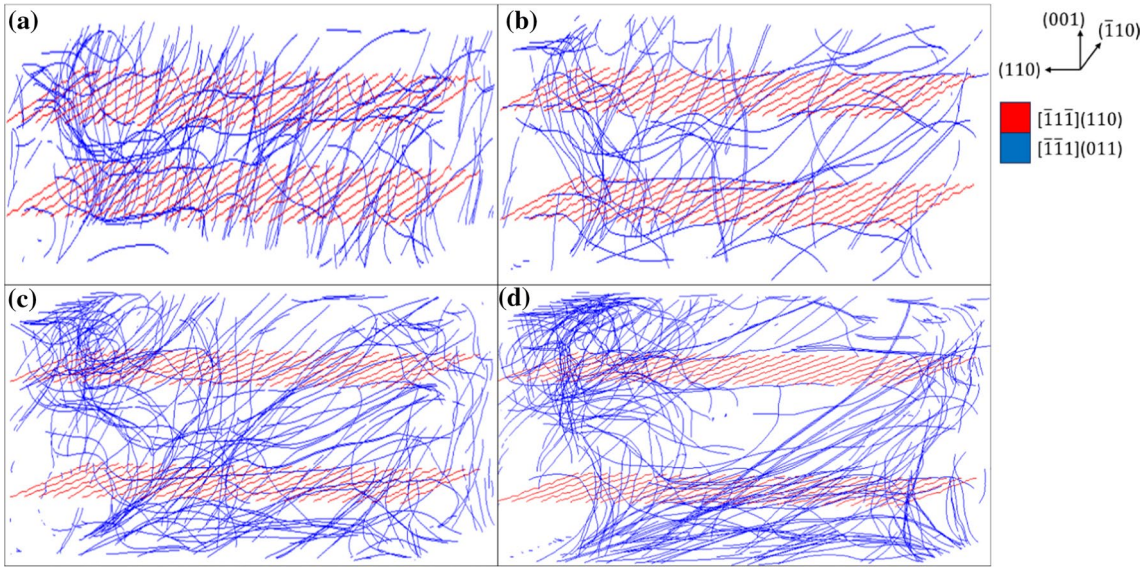

Figure 11 Final microstructural configurations for **a** 0.2 µm, **b** 0.3 µm, **c** 0.4 µm, and **d** 0.5 µm.

a valid assumption. It must be noted that the initial dislocation densities in [42] are somewhat larger, starting from larger initial densities. Another key aspect to note regarding the reported dislocation densities for the lath structure is that the values reported are the total dislocation densities which include mobile, immobile, and grain boundary dislocations. The literature regarding the reported dislocation densities in lath martensite is not 100% clear if it pertains to mobile/immobile dislocations or grain boundary dislocations. For example, [19] states that the initial dislocation density for the studied low-nickel lath martensite steel is approximately 3.8×10^{14} m^{-2}, and no distinction is made between mobile/immobile and grain boundary dislocations. Even in EBSD investigations [6, 18], no distinction is made between mobile/immobile and grain boundary dislocation densities.

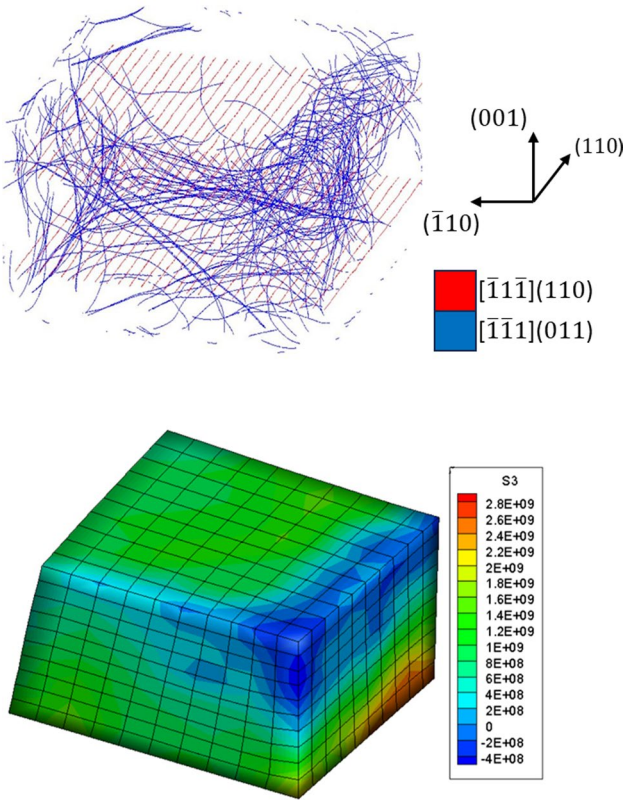

Figure 12 **a** Pile up (shown inside black oval) snapshot taken from the 0.5-µm scenario and **b** stress contour showing the effect of the pile up (units in Pa).

Packet–block simulations

Mechanical response

The K–S orientation relationship outlined in "Methodology" section was implemented in MDDP as illustrated in Fig. 3. The RVE represents a packet divided into two blocks or variants, namely, the V_1 and V_2 variants. The simulations were conducted at 300 K using a constant strain rate of 10^5 s^{-1}. Analyzing the stress–strain diagrams for the packet–block configurations in Fig. 14a reveals the following features:

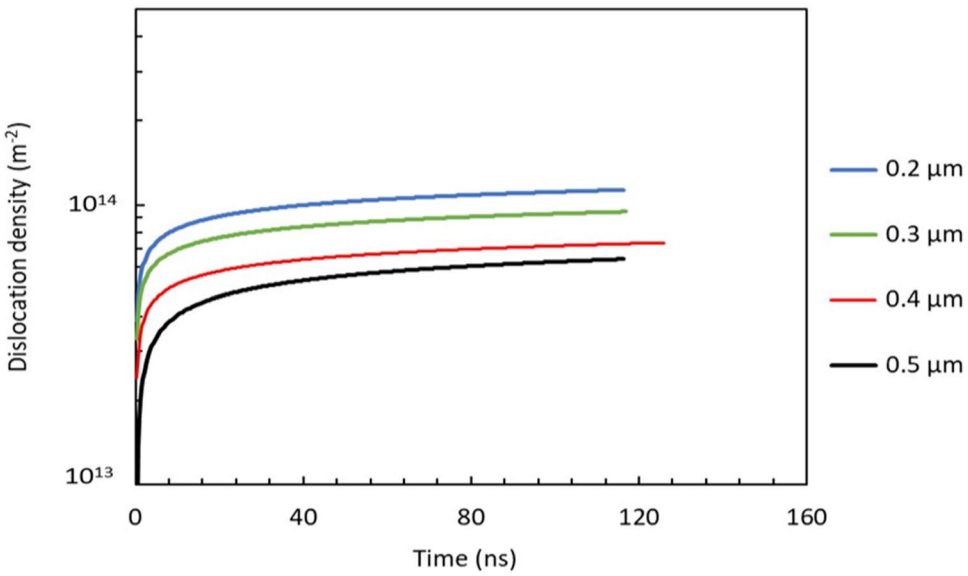

Figure 13 Dislocation density evolution over time comparison for $D = 0.2$-µm, 0.3-µm, 0.4-µm, and 0.5-µm lath widths.

1. Initially, the behavior is linear elastic up to the onset of yielding.
2. Following yielding, plastic flow is initiated after a drop in stress via mass cross-slip, i.e., a dislocation avalanche has taken place where secondary slip systems of the type < 112 > are activated, therefore indicating plastic relaxation. The observed elastic overshoot in all samples is most likely attributed to the high strain rate used in this study [1].
3. Gradual strain hardening is observed afterwards due to the cross-slipped dislocations piling up at both the packet and block boundaries. The effect of the hardening is balanced by relaxation processes, namely, more cross-slip, resulting in the stress magnitude being kept almost constant.
4. The samples undergo further relaxation. The process of relaxation is attributed to another cross-slip event where dislocations cross slip on both the primary slip systems of the type < 110 > and secondary < 112 > slip systems of the type.

The dislocation avalanche and cross-slip events are evidenced by observing how the dislocation density changes and evolves over time as shown in Fig. 14b. Dislocation density starts to increase slightly once the critical resolved shear stress value is reached, and the dislocations start to bow out and multiply through the FR mechanism. Yielding is marked by a sharp increase in dislocation density therefore evidencing the presence of a dislocation avalanche which can occur through cross-slip. The dislocation density then reaches a plateau resulting in S-shaped dislocation density curves. When a sufficient number of dislocations have piled up against the block boundary, then dislocations cross slip en masses and cause a dislocation avalanche, thus balancing out the hardening that was occurring due to dislocation multiplication and pile up.

Microstructural evolution and its effect on the mechanical response

The underlying microstructural processes are the main drive behind the observed macro-scale response of a material. The main microstructural features detected in the simulations are dislocation pile up at packet and block boundaries and cross-slip. The dislocation pile up is first apparent once the FR source is activated, and dislocation multiplication takes place as shown in Fig. 15. The resulting dislocations start to pile up against the grain boundaries. Dislocations are piling up next to each other, as well as on top of each other later on during the loading process as will be shown shortly. As the stress increases, the second microstructural feature comes into light. Yielding occurs via dislocations undergoing cross-slip en masse or dislocation avalanche. It is known that dislocations tend to cross slip at boundaries as evidenced by the findings of [13] where the dislocations cross slip into the (312) plane. However, as the simulations show, dislocations also cross slip into the $(\overline{112})$ and the $(\overline{121})$ secondary slip

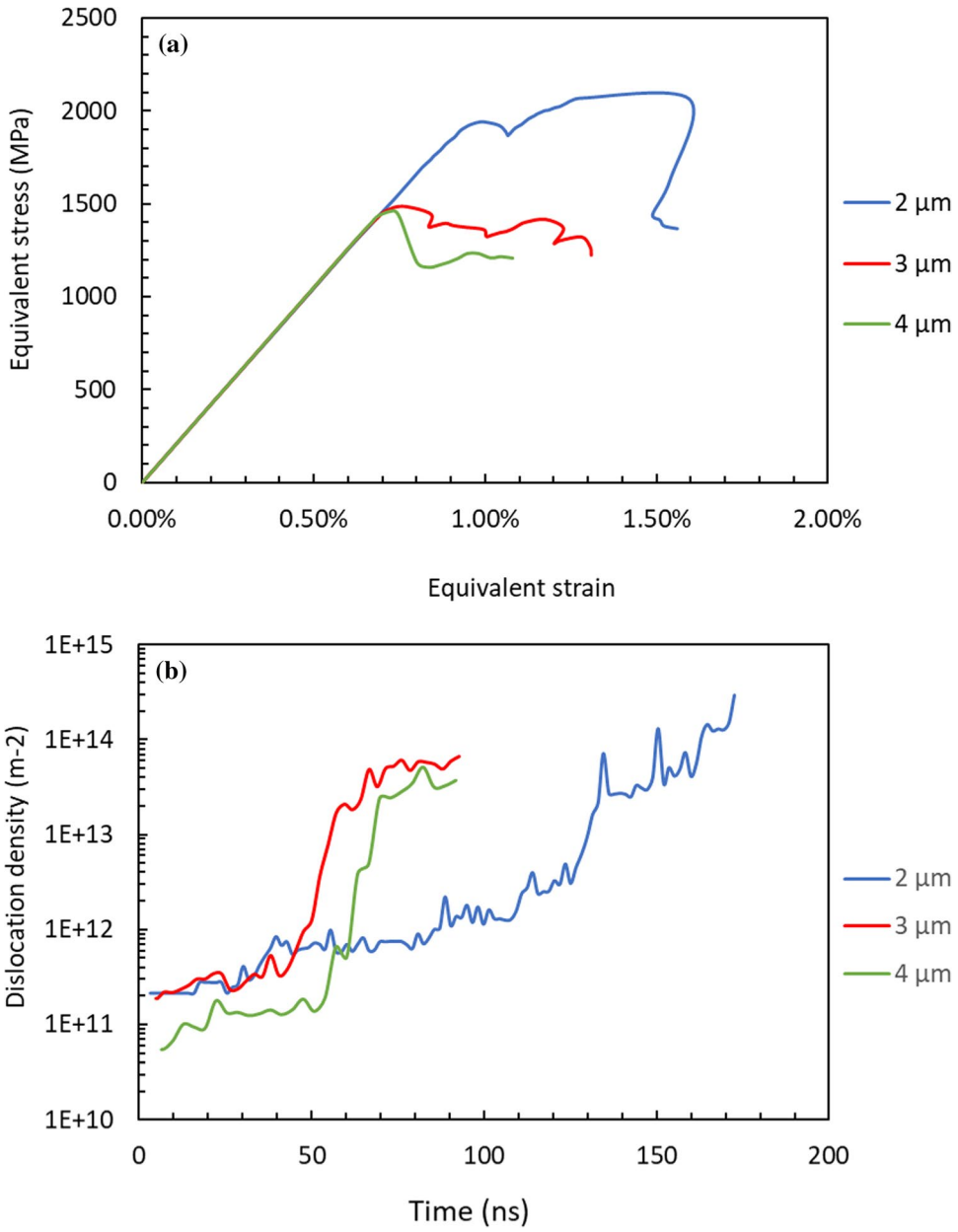

Figure 14 **a** Stress–strain diagram depicting the mechanical response of the samples subject to uniaxial tension. The material is linear elastic up to yielding after which it undergoes plastic relaxation followed by a gradual hardening that is then followed by more relaxation. **b** Dislocation density evolution over time. Once dislocation multiplication takes place, the dislocation density slightly increases, which is followed by an abrupt surge in dislocation density which suggests that a dislocation avalanche has occurred. The dislocation density then plateaus until the next dislocation avalanche happens which results in another sharp increase.

systems which are activated resulting in a dislocation avalanche as shown in Fig. 16a. These findings are validated by [35] who used EBSD scans of as-quenched lath martensite, subjected to uniaxial tensile deformation to prove that the activation of the primary slip systems {110} < 111 > takes precedence over the secondary slip, namely, the {112} < 111 > slip systems, up to 20% elongation and that the lath structure is maintained during the tensile tests. The MDDP model was capable of detecting the activation of the secondary slip systems, and as discussed in "Lath boundaries" section, since the lath boundaries only experience local deformation in the form of jogs, their overall structure was maintained as suggested by Michiuchi. Following the dislocation avalanche, the dislocations then glide freely through the crystal until they hit the grain boundaries and start piling up next to each other leading to material hardening. This hardening is then balanced by a relaxation process in the form of another cross-slip where the dislocations on the $(\overline{112})$ and the $(\overline{121})$ resulting from the initial cross-slip themselves cross slip into the {110} and {112} type slip planes. These dislocations then pile up next to each other and on top of previously

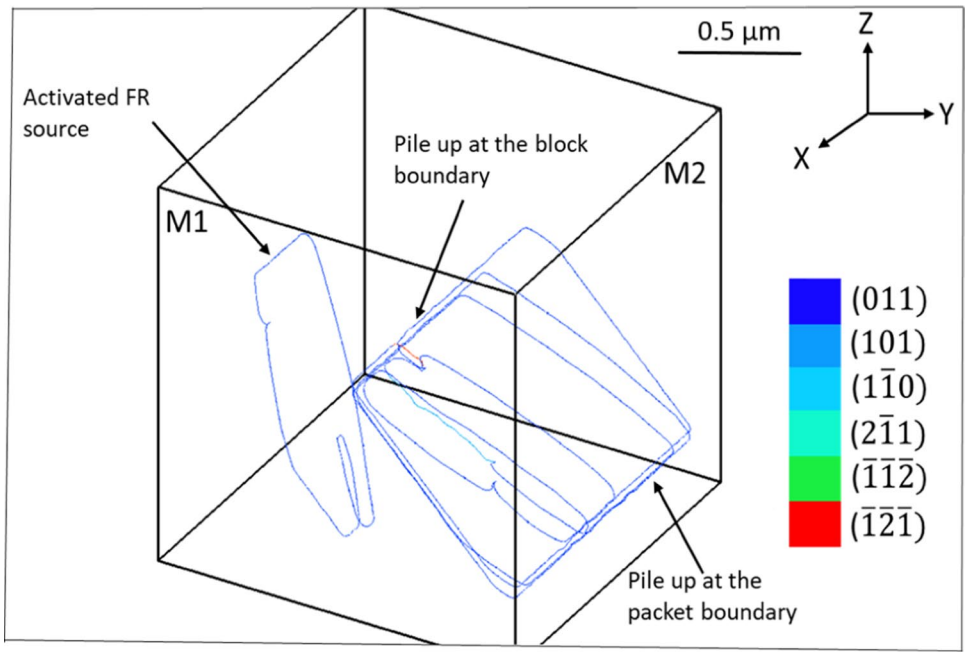

Figure 15 Frank–Read source activation and initial dislocation pile up.

cross-slipped dislocations as depicted in Fig. 16b and **16**c, respectively. [7] calculated the critical resolved shear stress (CRSS) for {110}, {211}, and {123} slip plane families that activate during micro-tensile tests and found that $CRSS_{\{110\}} < CRSS_{\{211\}} < CRSS_{\{123\}}$, meaning that it is easier for dislocations to slip on the {110} planes than it is to slip on the {211} and {123} slip planes. In the MDDP simulations, dislocation slip occurred on the (011), ($\overline{112}$) and the ($\overline{121}$) slip planes, which is in agreement with the experimental results of [7].

Effect of initial dislocation density

Carbon content and thermomechanical processing strongly affect the initial dislocation density [20, 49, 57]. The carbon atoms segregate on the lath boundaries which then increase the dislocation density. Different thermomechanical processing affects the initial dislocation density, where following the martensitic transformation a tempering process is applied to reduce impurities and therefore decrease the initial dislocation density. The initial dislocation density of lath martensitic steels depends strongly on the heat treatment and thermomechanical processing with values ranging from 10^{12} to 10^{14} m^{-2} for different thermal processing conditions [25, 41].

For computational purposes, the initial dislocation density used in this hovers around 10^{11} m^{-2}. To examine the effect of different initial dislocation densities on the mechanical response, three scenarios are devised for this purpose. Three different initial dislocation densities, 2×10^{11} m^{-2} and 7×10^{11} m^{-2} and 10^{12} m^{-2}, are utilized to determine whether or not the initial dislocation density has any effect on the mechanical response.

Increasing the initial dislocation density has no noticeable effect on the microstructure evolution and the main microstructural features that arise during plastic deformation (pile up and cross-slip). However, as per the Bailey–Hirsh relation, the yield stress is related to the square root of the dislocation density [3]. The stress–strain diagrams of the considered cases are shown in Fig. 17a. It can be seen that the yield point varies slightly between the three cases due to the different dislocation densities between all three simulations. Plastic behavior is fairly similar in all three cases where hardening is balanced by relaxation via cross-slip. Figure 17b depicts the dislocation density evolution over time. All three curves follow the same S-shaped trend. The 7×10^{11} and 10^{12} m^{-2} scenarios exhibit a higher final dislocation density following yielding due to those two cases having two and three initial FR sources, therefore resulting in more dislocations being emanated from the FR sources which then pile up at the boundaries. Pile ups cause an increase in dislocation density. The increased number of piled up dislocations leads

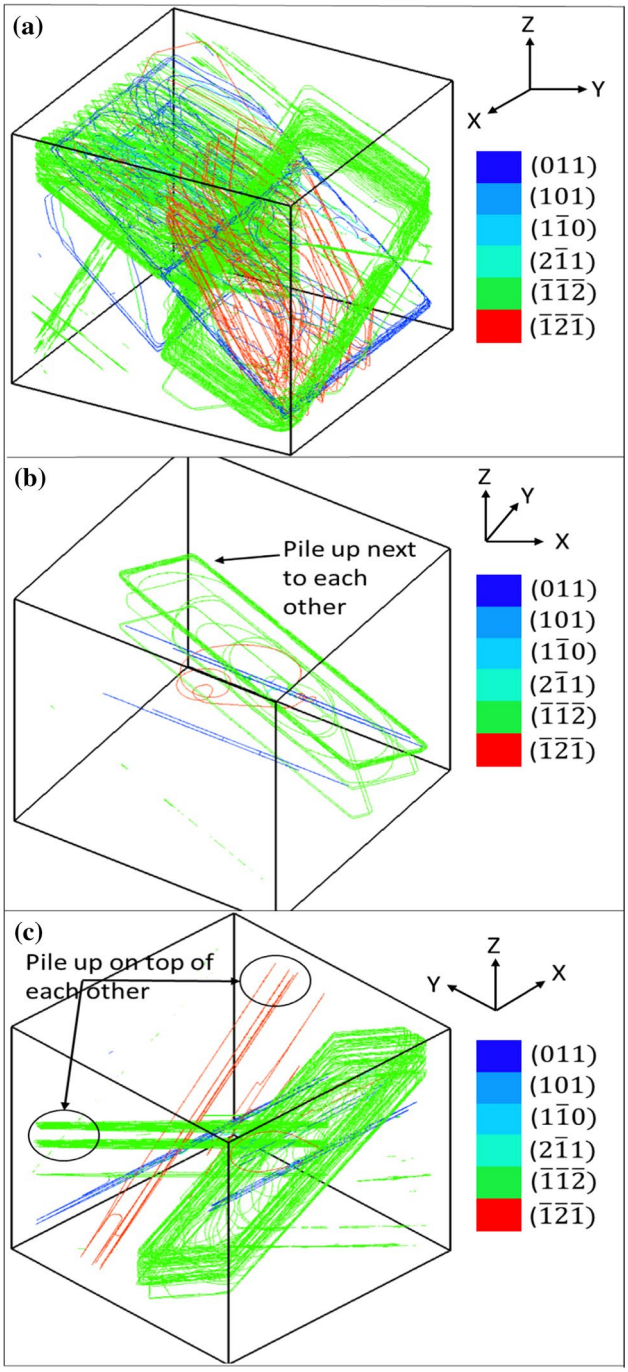

Figure 16 **a** Dislocation avalanche as a result of mass cross-slip from the initial dislocations on the (011) slip plane and **b** cross-slip which is responsible for dislocation avalanche leading to plastic relaxation in the samples. Cross-slipped dislocations pile up next to each other against packet and block boundaries leading to material hardening. **c** Dislocations piling up on top of each other.

to more dislocations undergoing cross-slip, therefore, an additional increase in dislocation density and higher final dislocation densities than the 2×10^{11} m^{-2}.

Precipitates and their effect on the plastic behavior

$M_{23}C_6$ carbides are believed to be the most important precipitates in P91 martensitic steel and are located on the lath boundaries. Due to the importance of precipitates, the role they play on the mechanical response of the material merits an investigation. The precipitate diameter used is $D_p = 200$ nm, and the precipitate spacing $L_p = 571$ nm which is a mean value used based on the findings of D. F. Li et al., 2014b. Lath boundaries are ignored since they have no effect on material flow as demonstrated in "Mechanical response" section. Precipitates are placed where lath boundaries ought to be since $M_{23}C_6$ carbides are located on lath boundaries, as shown in Fig. 3 which depicts the simulation setup for the precipitate investigation. Figure 18 shows a schematic of the dislocation interaction with the precipitate, and how Orowan loops are formed. Precipitates are implemented in MDDP as "frictional spheres" similarly to the way, grain boundaries were modeled. To elaborate on how the precipitates are modeled, precipitates are considered as impenetrable spheres. Similar to how a very high frictional force was applied on a plane to model the impenetrable boundaries, a very high frictional force is applied inside of the RVE and its effect is limited to the locations of the precipitates. A 2-μm packet divided into two 1-μm blocks, namely, the $V1$ and $V2$ variants used in the simulations above. The sample is subjected to uniaxial tension, and the boundary conditions are the same as previous simulations.

Figure 19 compares the mechanical response of two 2-μm samples, one where precipitates with diameter $D_p = 200$ nm and separated by a distance $L_P = 571$, and the other sample where precipitates were not considered. The presence of precipitates does not have any noticeable effect on the yield strength of the material. However, the presence of precipitates seems to trigger cross-slip at an earlier stage in the loading process. That is, due to the presence of precipitates, cross-slip happens earlier than it would have in the case where there is no precipitates, thus earlier stress relaxation occurs. This mechanism is further confirmed by [48] that made use of three-dimensional DDD simulations

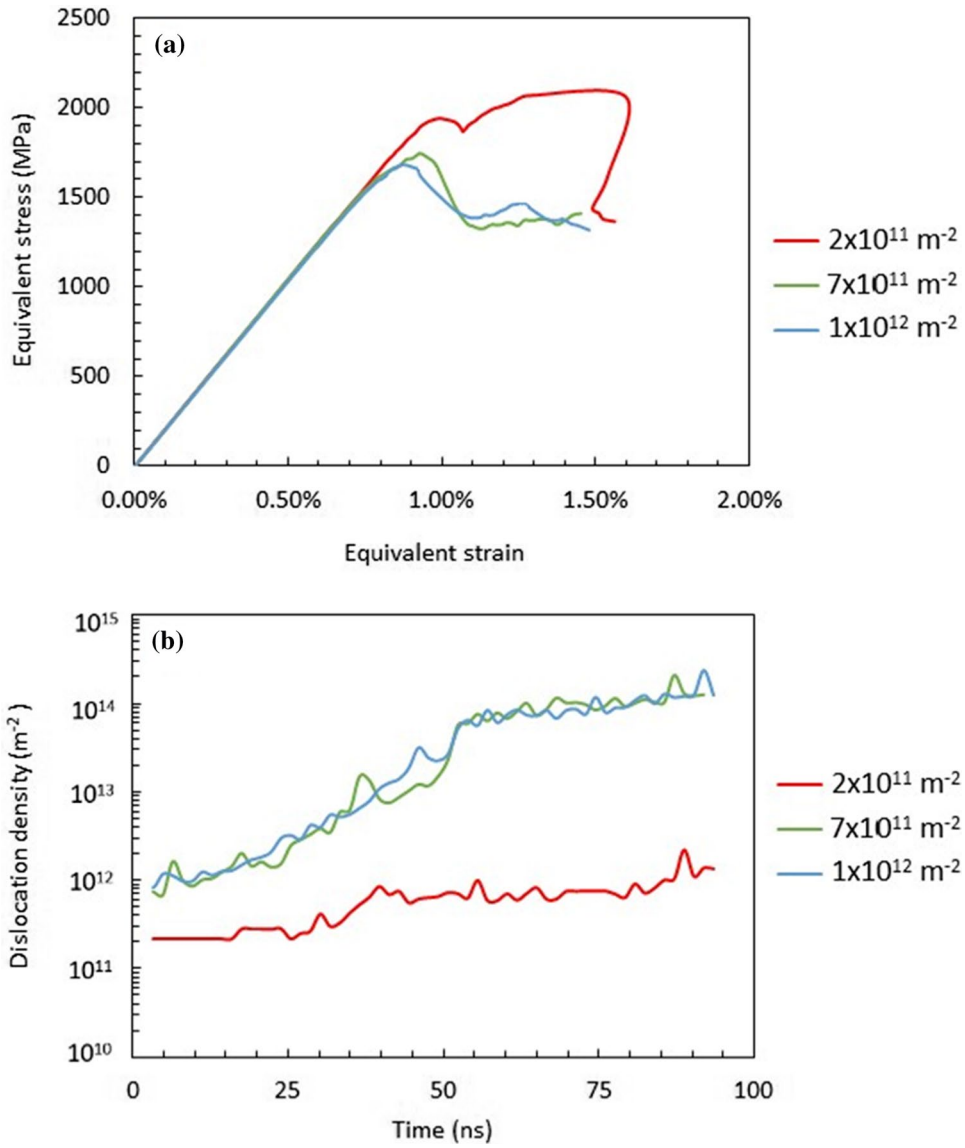

Figure 17 **a** Stress–strain curves for different initial dislocation densities 2×10^{11} m^{-2} and 7×10^{11} m^{-2} and 10^{12} m^{-2}. **b** Dislocation density evolution over time for the three different initial dislocation density cases.

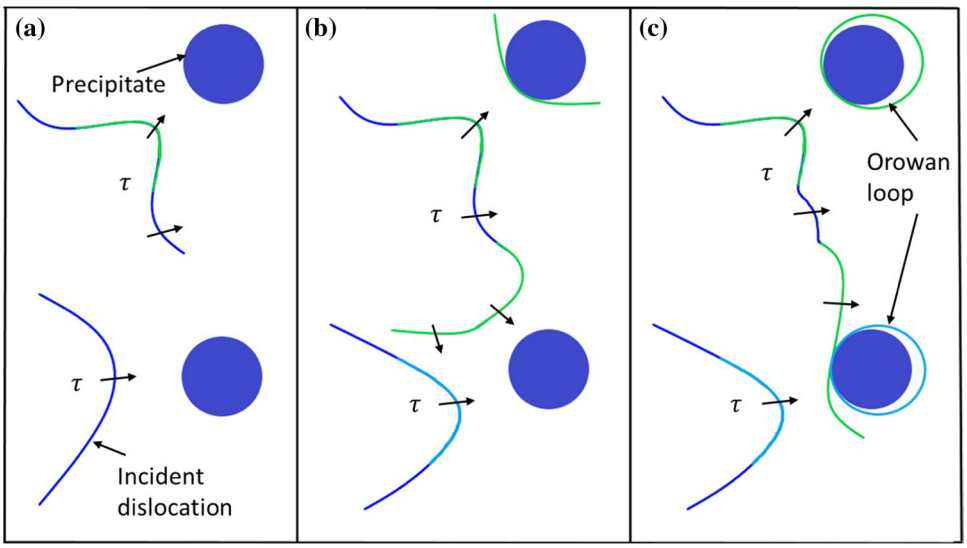

Figure 18 **a** Incident dislocations with one of them undergoing cross-slip (green). **b** Cross-slipped dislocation (green) looping around a precipitate. **c** Cross-slipped dislocations (green and light blue) will undergo the Orowan looping mechanism instead of pushing their way through the dislocation network in between the precipitates.

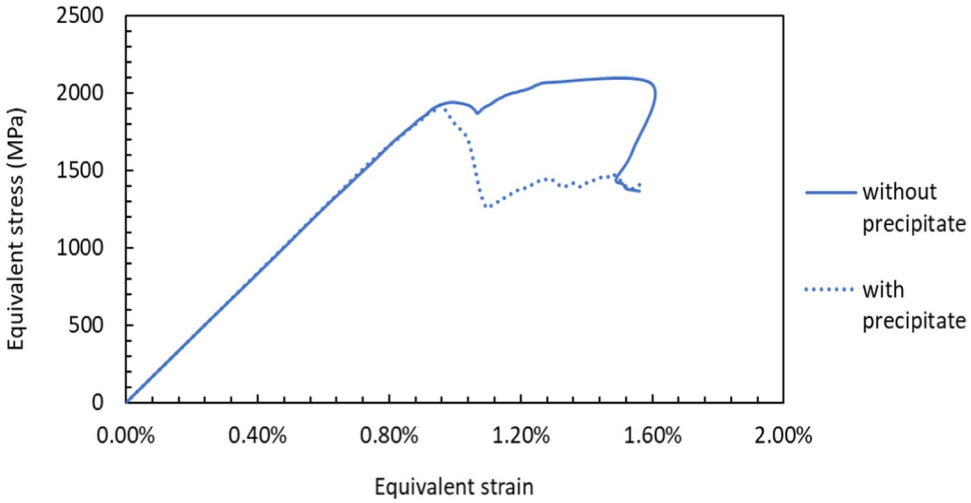

Figure 19 Stress–strain diagram for two scenarios, one with precipitates and one without precipitates.

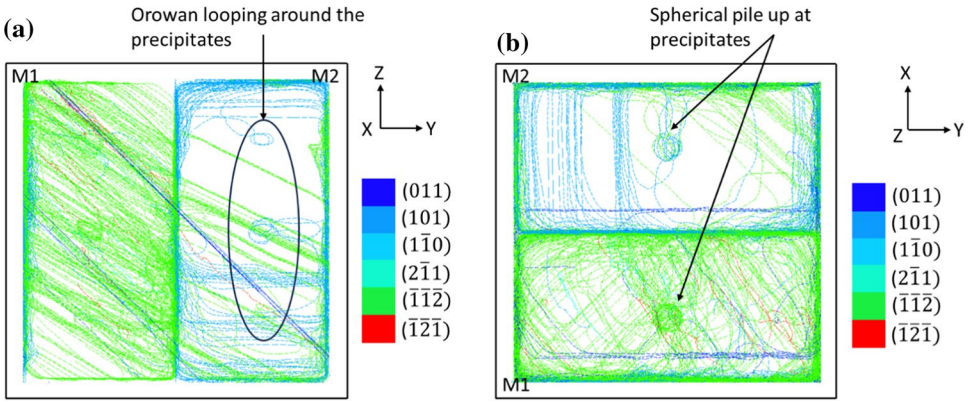

Figure 20 Snapshots of the material microstructure depicting the pile up at regions near the precipitates from **a** the front view and **b** the top view.

to prove that dislocations can bypass particles by cross-slip. As more dislocations loop around the precipitate, the probability of cross-slip increases since the stress required to make a dislocation glide between the precipitates that have Orowan loops around them becomes higher as the precipitate gets harder. In other words, it is energetically favorable for the dislocation to cross slip than it is to force its way in between hardened precipitates. This process is schematically shown in the figure below.

Dislocation interaction with precipitate is complex and depends on many factors such as the size and shape of the precipitate, separation distance between precipitates, the mismatch in the elastic properties of the matrix and the precipitate materials, and the mismatch in the stacking fault energies between the two materials. In general, two scenarios of dislocation–precipitate interaction are possible: (i) The dislocation cuts through the precipitate via shear, and (ii) the dislocation fully loops around the precipitate (Orowan looping), indicating the existence of impenetrable precipitates. Among other things, the combination of their size and separation distance makes the $M_{23}C_6$ carbide precipitates impenetrable. Thus, when the incident dislocations come in contact with $M_{23}C_6$ precipitates, their motion will be hindered and eventually stopped at the vicinity of the precipitate allowing Orowan looping to take place [2, 4, 29, 53]. When dislocations encounter impenetrable precipitates, they tend to loop around them leaving behind residues of dislocation loops that interact with glissile dislocations. With the glide of more dislocations during plastic flow, dislocations are bound to interact with the precipitates which lead to dislocation pile up and material hardening. Figure 18 shows the microstructural configuration at the end of the simulation where the plastic strain reached about 0.7%. By observing the material microstructure, it is seen that multiple dislocation loops have formed around precipitates which

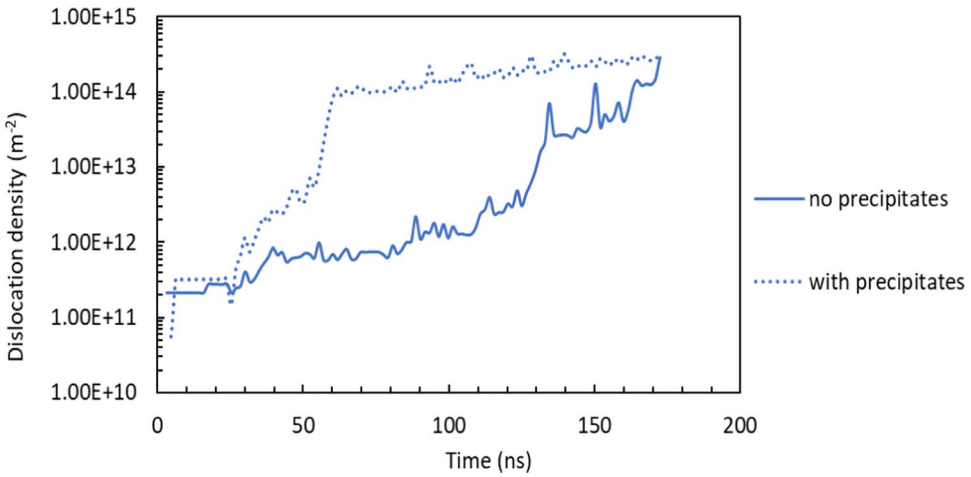

Figure 21 Comparison of the evolution of the dislocation density over time between the case without precipitates and the case with precipitates. The stress–strain diagrams exhibit three distinct phases. The first where dislocation density is constant and the material has not yielded, the second after yielding where a dislocation avalanche due to cross-slip results in a sharp increase in dislocation density, and finally, the third where dislocation density has reached saturation.

Figure 22 Size effect in lath martensitic steel.

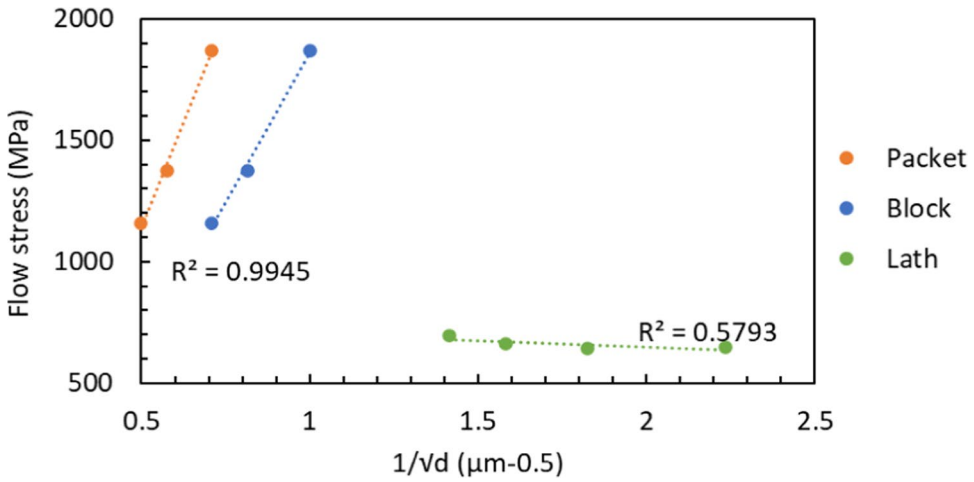

is in accordance with Orowan looping mechanism as shown in Fig. 20 [28].

The effect that precipitates have on the material is made clear by examining the dislocation density evolution of the two considered scenarios. The presence of precipitates in the material acts as an obstacle to dislocation motion as discussed above. Precipitates tend to bow dislocations around them and cause a spherical pile up which is evidenced by an increase in dislocation density that is sharper than the case with no precipitates. This sharp increase in dislocation density, as observed in Fig. 21, in the case with precipitates occurs at approximately 30 ns into the deformation while the increase in dislocation density occurs at around 50 ns into the loading process for the case without precipitates. The sudden increase in dislocation density is evidence of the cross-slip occurring within the material and of the dislocation pile up at the precipitates. The dislocation density curves show three distinct phases. The first phase where the dislocation density is constant, the second phase representing cross-slip and dislocation pile up where the dislocation density increases, and finally, the third phase where there is saturation. In order to fully understand the role that precipitates play in material strengthening, further simulations are required where different precipitate spacings L_p and precipitate diameters D_p are used.

Size effects

The strength of lath martensitic steel was analyzed as a function of the block and packet size is considered as the effective grain size as shown in Fig. 22. By examining the flow stresses and plotting those values as a function of $1/\sqrt{d_{\text{packet}}}$ and $1/\sqrt{d_{\text{block}}}$, where d_{packet} and d_{block} are the packet and block sizes, respectively. It is seen that the flow stress is directly proportional to $1/\sqrt{d}$ via a linear equation of the form $\sigma_{\text{flow}}(\varepsilon) = \sigma_0 + k(\varepsilon)d^{-0.5}$ indicating that a Hall–Petch type relation exists for the material when the packet or block sizes are considered as the effective grain size.

One must note, however, that depending on the manufacturing process of lath martensitic steels, the packet size may increase up to hundreds of microns while the block size reaches only 10 μm. The lath width has been shown to have no effect on the flow stress of the material, meaning that so size effect has been observed when considering the lath width as the effective grain size. Therefore, the block size should be chosen as the main parameter for size effect investigations, a fact confirmed by Voronoi tessellation strain gradient crystal plasticity-based simulations carried out by [51].

Summary

The microstructure of a P91 martensitic steel was modeled and analyzed according to the K–S orientation relationship in MDDP for two martensite variants. The dislocation interactions with GBs have been examined in relation to the mechanical response of the material. Results have shown that the lath boundaries have no significant effect on the plasticity mechanisms of the material and pose little to no obstacle to dislocation motion. The dominant mechanisms of plastic deformation were found to be crystallographic slip including glide and cross-slip which occurs after dislocation pile up at packet and block boundaries. The initial dislocation density does not affect the plastic behavior of the material. The block size was found to be the most important structural parameter when analyzing the strength of martensitic steels. Future work will examine in detail the effect of precipitate size and spacing on the mechanical response and expanding the K–S relationship to more than two variants. Implementing the K–S orientation relationship allows for the simulation of two grains with different orientations.

The results of this study pave the way for researchers to simulate polycrystalline microstructures using DDD simulations. The insights gained from studying P91 martensitic steel shed light on crucial aspects of its mechanical behavior and deformation mechanisms, providing key information for engineering its microstructure in practical applications. Its most notable applications is in power plants where its superior creep resistance is leveraged. The significance of the block in the mechanical behavior of the steel and the role lath boundaries play in the plastic deformation of P91 steel can inform and enhance macroscopic plasticity models, thus bridging the gap between micro- and macro-scale phenomena in materials science.

Acknowledgements

Support from the Office or Research and Innovation at Alfaisal University and the Research Board at the American University of Beirut is greatly acknowledged. The authors would like to acknowledge the helpful discussion with Dr. Noel O'Dowd (University of Limerick).

Author contributions

OAAM and MS have contributed equally to this work.

Data and code availability

All data can be made available to interest readers upon request.

Declarations

Conflict of interest The authors declare that they have no conflict of interest.

Ethical approval Not applicable.

Appendix

See Tables 3 and 4.

Table 3 The 24 crystallographic variants for the K–S orientation relationship [23]

Variant	Plane parallel	Direction parallel
V1	$(111)_{\gamma}//(011)_{\alpha'}$	$[\bar{1}01]_{\gamma}//[\bar{1}\bar{1}1]_{\alpha'}$
V2		$[\bar{1}01]_{\gamma}//[\bar{1}1\bar{1}]_{\alpha'}$
V3		$[01\bar{1}]_{\gamma}//[\bar{1}\bar{1}1]_{\alpha'}$
V4		$[01\bar{1}]_{\gamma}//[\bar{1}1\bar{1}]_{\alpha'}$
V5		$[1\bar{1}0]_{\gamma}//[\bar{1}\bar{1}1]_{\alpha'}$
V6		$[1\bar{1}0]_{\gamma}//[\bar{1}1\bar{1}]_{\alpha'}$
V7	$(1\bar{1}1)_{\gamma}//(011)_{\alpha'}$	$[10\bar{1}]_{\gamma}//[\bar{1}\bar{1}1]_{\alpha'}$
V8		$[10\bar{1}]_{\gamma}//[\bar{1}1\bar{1}]_{\alpha'}$
V9		$[\bar{1}\bar{1}0]_{\gamma}//[\bar{1}\bar{1}1]_{\alpha'}$
V10		$[\bar{1}\bar{1}0]_{\gamma}//[\bar{1}1\bar{1}]_{\alpha'}$
V11		$[011]_{\gamma}//[\bar{1}\bar{1}1]_{\alpha'}$
V12		$[011]_{\gamma}//[\bar{1}1\bar{1}]_{\alpha'}$
V13	$(\bar{1}11)_{\gamma}//(011)_{\alpha'}$	$[0\bar{1}1]_{\gamma}//[\bar{1}\bar{1}1]_{\alpha'}$
V14		$[0\bar{1}1]_{\gamma}//[\bar{1}1\bar{1}]_{\alpha'}$
V15		$[\bar{1}0\bar{1}]_{\gamma}//[\bar{1}\bar{1}1]_{\alpha'}$
V16		$[\bar{1}0\bar{1}]_{\gamma}//[\bar{1}1\bar{1}]_{\alpha'}$
V17		$[110]_{\gamma}//[\bar{1}\bar{1}1]_{\alpha'}$
V18		$[110]_{\gamma}//[\bar{1}1\bar{1}]_{\alpha'}$
V19	$(11\bar{1})_{\gamma}//(011)_{\alpha'}$	$[\bar{1}10]_{\gamma}//[\bar{1}\bar{1}1]_{\alpha'}$
V20		$[\bar{1}10]_{\gamma}//[\bar{1}1\bar{1}]_{\alpha'}$
V21		$[0\bar{1}\bar{1}]_{\gamma}//[\bar{1}\bar{1}1]_{\alpha'}$
V22		$[0\bar{1}\bar{1}]_{\gamma}//[\bar{1}1\bar{1}]_{\alpha'}$
V23		$[101]_{\gamma}//[\bar{1}\bar{1}1]_{\alpha'}$
V24		$[101]_{\gamma}//[\bar{1}1\bar{1}]_{\alpha'}$

Table 4 Misorientation angles between ***V*1** and the other martensitic variants [23]

Variant	Misorientation angle from *V*1 (°)
V1	–
V2	60
V3	60
V4	10.53
V5	60
V6	49.47
V7	49.47
V8	10.53
V9	50.51
V10	50.51
V11	14.88
V12	57.21
V13	14.88
V14	50.51
V15	57.21
V16	20.61
V17	51.73
V18	47.11
V19	50.51
V20	57.21
V21	20.61
V22	47.11
V23	57.21
V24	21.06

References

[1] An W, Zeng Z, Xiong Q, Huang M, Li Z (2023) Crystal plasticity study of stress overshoot during high-strain rate deformation. Meccanica 58:193–215. https://doi.org/10.1007/s11012-022-01632-3

[2] Azeem MM, Wang Q, Li Z, Zhang Y (2020) Dislocation-oxide interaction in Y2O3 embedded Fe: a molecular dynamics simulation study. Nucl Eng Technol 52:337–343. https://doi.org/10.1016/J.NET.2019.07.011

[3] Bailey JE, Hirsch PB (1960) The dislocation distribution, flow stress, and stored energy in cold-worked polycrystalline silver. Philos Mag A J Theor Exp Appl Phys 5:485–497. https://doi.org/10.1080/14786436008238300

[4] Bakó B, Weygand D, Samaras M, Chen J, Pouchon MA, Gumbsch P, Hoffelner W (2007) Discrete dislocation dynamics simulations of dislocation interactions with Y2O3 particles in PM2000 single crystals. Philos Mag 87:3645–3656. https://doi.org/10.1080/14786430701383085

[5] Barrett RA, O'Donoghue PE, Leen SB (2014) A dislocation-based model for high temperature cyclic viscoplasticity of 9–12Cr steels. Comput Mater Sci 92:286–297. https://doi.org/10.1016/j.commatsci.2014.05.034

[6] Berecz T, Jenei P, Csóré A, Lábár J, Gubicza J, Szabó PJ (2016) Determination of dislocation density by electron backscatter diffraction and X-ray line profile analysis in ferrous lath martensite. Mater Charact 113:117–124. https://doi.org/10.1016/j.matchar.2015.11.014

[7] Deschênes PA, Wheeler R, Paquet D, Lanteigne J, Serventi AM, Tôn-Thât L, Champliaud H (2022) Micromechanical properties of low-carbon martensitic stainless steel by microtensile experiments. Mater Sci Eng A 858:144030. https://doi.org/10.1016/J.MSEA.2022.144030

[8] Du C, Hoefnagels JPM, Vaes R, Geers MGD (2016) Block and sub-block boundary strengthening in lath martensite. Scr Mater 116:117–121. https://doi.org/10.1016/j.scriptamat.2016.01.043

[9] El Ters P, Shehadeh MA (2023) On the investigation of size effect in bcc α-iron under high strain rate and high temperature: multiscale dislocations dynamics simulations. Eur J Mech-A/Solids 97:104779. https://doi.org/10.1016/j.euromechsol.2022.104779

[10] El Ters P, Shehadeh MA (2020) On the strain rate sensitivity of size-dependent plasticity in BCC iron at elevated temperatures: discrete dislocation dynamics investigation. Mech Mater 148:103494. https://doi.org/10.1016/j.mechmat.2020.103494

[11] El Ters P, Shehadeh MA (2019) Modeling the temperature and high strain rate sensitivity in BCC iron: atomistically informed multiscale dislocation dynamics simulations. Int J Plast 112:257–277. https://doi.org/10.1016/j.ijplas.2018.09.002

[12] Gao Y, Zhuang Z, You X (2011) A hierarchical dislocation-grain boundary interaction model based on 3D discrete dislocation dynamics and molecular dynamics. Sci China Phys Mech Astron 54:625–632. https://doi.org/10.1007/s11433-011-4298-9

[13] Ghaffarian H, Na YE, Jang D (2022) Interfacial plasticity mediated by lath boundaries in reduced-activation ferritic/martensitic steels. J Nucl Mater 559:153439. https://doi.org/10.1016/j.jnucmat.2021.153439

[14] Ghassemi-Armaki H, Maaß R, Bhat SP, Sriram S, Greer JR, Kumar KS (2014) Deformation response of ferrite and martensite in a dual-phase steel. Acta Mater 62:197–211. https://doi.org/10.1016/j.actamat.2013.10.001

[15] Golden BJ, Tiernan P, Scully S, (2016) PVP2015–45487 pp 1–9

[16] Gurrutxaga-Lerma B (2016) The role of the mobility law of dislocations in the plastic response of shock loaded pure metals. Model Simul Mater Sci Eng 24:065006. https://doi.org/10.1088/0965-0393/24/6/065006

[17] Gurrutxaga-Lerma B, Shehadeh MA, Balint DS, Dini D, Chen L, Eakins DE (2017) The effect of temperature on the elastic precursor decay in shock loaded FCC aluminium and BCC iron. Int J Plast 96:135–155. https://doi.org/10.1016/j.ijplas.2017.05.001

[18] HajyAkbary F, Sietsma J, Böttger AJ, Santofimia MJ (2015) An improved X-ray diffraction analysis method to characterize dislocation density in lath martensitic structures. Mater Sci Eng A 639:208–218. https://doi.org/10.1016/j.msea.2015.05.003

[19] Hatem TM, Zikry MA (2009) Dislocation density crystalline plasticity modeling of lath martensitic microstructures in steel alloys. Philos Mag 89:3087–3109. https://doi.org/10.1080/14786430903185999

[20] Hutchinson B, Hagström J, Karlsson O, Lindell D, Tornberg M, Lindberg F, Thuvander M (2011) Microstructures and hardness of as-quenched martensites (0.1–0.5%C). Acta Mater 59:5845–5858. https://doi.org/10.1016/J.ACTAMAT.2011.05.061

[21] Jiang M, Monnet G, Devincre B (2021) On the origin of the Hall–Petch law: a 3D-dislocation dynamics simulation investigation. Acta Mater 209:116783. https://doi.org/10.1016/j.actamat.2021.116783

[22] Khan SMA, Zbib HM, Hughes DA (2004) Modeling planar dislocation boundaries using multi-scale dislocation dynamics plasticity. Int J Plast 20:1059–1092. https://doi.org/10.1016/j.ijplas.2003.10.004

[23] Kitahara H, Ueji R, Tsuji N, Minamino Y (2006) Crystallographic features of lath martensite in low-carbon steel. Acta Mater 54:1279–1288. https://doi.org/10.1016/j.actamat.2005.11.001

[24] Kitahara H, Ueji R, Ueda M, Tsuji N, Minamino Y (2005) Crystallographic analysis of plate martensite in Fe-28.5 at% Ni by FE-SEM/EBSD. Mater Charact 54:378–386. https://doi.org/10.1016/j.matchar.2004.12.015

[25] Klueh RL (2005) Elevated temperature ferritic and martensitic steels and their application to future nuclear reactors. Int Mater Rev 50:287–310. https://doi.org/10.1179/174328005X41140

[26] Kondo S, Mitsuma T, Shibata N, Ikuhara Y (2016) Direct observation of individual dislocation interaction processes with grain boundaries. Sci Adv 2:1–8. https://doi.org/10.1126/sciadv.1501926

[27] Kurdjumow G, Sachs G (1930) Der Mechanismus der Stahlhärtung Naturwissenschaften 18:534. https://doi.org/10.1007/BF01513427

[28] Li DF, Golden BJ, O'Dowd NP (2014) Multiscale modelling of mechanical response in a martensitic steel: a

micromechanical and length-scale-dependent framework for precipitate hardening. Acta Mater 80:445–456. https://doi.org/10.1016/j.actamat.2014.08.012

[29] Li J, Liu B, Fang QH, Huang ZW, Liu YW (2017) Atomic-scale strengthening mechanism of dislocation-obstacle interaction in silicon carbide particle-reinforced copper matrix nanocomposites. Ceram Int 43:3839–3846. https://doi.org/10.1016/J.CERAMINT.2016.12.040

[30] Li S, Zhu G, Kang Y (2016) Effect of substructure on mechanical properties and fracture behavior of lath martensite in 0.1C-1.1Si-1.7Mn steel. J Alloys Compd 675:104–115. https://doi.org/10.1016/j.jallcom.2016.03.100

[31] Li Z, Hou C, Huang M, Ouyang C (2009) Strengthening mechanism in micro-polycrystals with penetrable grain boundaries by discrete dislocation dynamics simulation and Hall–Petch effect. Comput Mater Sci 46:1124–1134. https://doi.org/10.1016/j.commatsci.2009.05.021

[32] Luo H, Wang X, Liu Z, Yang Z (2020) Influence of refined hierarchical martensitic microstructures on yield strength and impact toughness of ultra-high strength stainless steel. J Mater Sci Technol 51:130–136. https://doi.org/10.1016/j.jmst.2020.04.001

[33] Maki T, Tsuzaki K, Tamura I (1980) The Morphology of Microstructure Composed of Lath Martensites in Steels. Trans Iron Steel Inst Japan 20:207–214. https://doi.org/10.2355/isijinternational1966.20.207

[34] Meade ED, Sun F, Tiernan P, O'Dowd NP (2018) Experimental study and multiscale modelling of the high temperature deformation of tempered martensite under multiaxial loading. Mater Sci Eng A 737:383–392. https://doi.org/10.1016/j.msea.2018.09.040

[35] Michiuchi M, Nambu S, Ishimoto Y, Inoue J, Koseki T (2009) Relationship between local deformation behavior and crystallographic features of as-quenched lath martensite during uniaxial tensile deformation. Acta Mater 57:5283–5291. https://doi.org/10.1016/J.ACTAMAT.2009.06.021

[36] Mine Y, Hirashita K, Takashima H, Matsuda M, Takashima K (2013) Micro-tension behaviour of lath martensite structures of carbon steel. Mater Sci Eng A 560:535–544. https://doi.org/10.1016/j.msea.2012.09.099

[37] Morito S, Tanaka H, Konishi R, Furuhara T, Maki T (2003) The morphology and crystallography of lath martensite in Fe–C alloys. Acta Mater 51:1789–1799. https://doi.org/10.1016/S1359-6454(02)00577-3

[38] Morito S, Yoshida H, Maki T, Huang X (2006) Effect of block size on the strength of lath martensite in low carbon steels. Mater Sci Eng A 438–440:237–240. https://doi.org/10.1016/j.msea.2005.12.048

[39] Na H, Nambu S, Ojima M, Inoue J, Koseki T (2014) Crystallographic and microstructural studies of lath martensitic steel during tensile deformation. Metall. Mater Trans A Phys Metall Mater Sci 45:5029–5043. https://doi.org/10.1007/s11661-014-2461-4

[40] Ohashi T, Kawamukai M, Zbib H (2007) A multiscale approach for modeling scale-dependent yield stress in polycrystalline metals. Int J Plast 23:897–914. https://doi.org/10.1016/J.IJPLAS.2006.10.002

[41] Pešička J, Kužel R, Dronhofer A, Eggeler G (2003) The evolution of dislocation density during heat treatment and creep of tempered martensite ferritic steels. Acta Mater 51:4847–4862. https://doi.org/10.1016/S1359-6454(03)00324-0

[42] Shamsujjoha M (2020) Evolution of microstructures, dislocation density and arrangement during deformation of low carbon lath martensitic steels. Mater Sci Eng A 776:139039. https://doi.org/10.1016/J.MSEA.2020.139039

[43] Shehadeh* MA, Zbib HM, Diaz De La Rubia T (2005) Modelling the dynamic deformation and patterning in fcc single crystals at high strain rates: dislocation dynamics plasticity analysis, Philos Mag, 85, 1667–1685. https://doi.org/10.1080/14786430500036470

[44] Shehadeh MA (2012) Multiscale dislocation dynamics simulations of shock-induced plasticity in small volumes. Philos Mag 92:1173–1197. https://doi.org/10.1080/14786435.2011.637988

[45] Shehadeh MA, El Ters P, Armstrong RW, Arnold W (2021) Dislocation mechanics of extremely high rate deformations in iron and tantalum. J Eng Mater Technol. https://doi.org/10.1115/1.4052104

[46] Shehadeh MA, Zbib HM, Diaz de la Rubia T (2005) Multiscale dislocation dynamics simulations of shock compression in copper single crystal. Int J Plast 21:2369–2390. https://doi.org/10.1016/j.ijplas.2004.12.004

[47] Shibata A, Nagoshi T, Sone M, Morito S, Higo Y (2010) Evaluation of the block boundary and sub-block boundary strengths of ferrous lath martensite using a micro-bending test. Mater Sci Eng A 527:7538–7544. https://doi.org/10.1016/j.msea.2010.08.026

[48] Shin CS, Fivel MC, Verdier M, Oh KH (2003) Dislocation–impenetrable precipitate interaction: a three-dimensional discrete dislocation dynamics analysis. Philos Mag 83:3691–3704. https://doi.org/10.1080/14786430310001599379

[49] Singh J, Nath SK (2020) Effects of cyclic heat treatment on microstructure and mechanical properties of 13%Cr–4%Ni Martensitic stainless steel. J Mater Eng Perform 29:2478–2490. https://doi.org/10.1007/s11665-020-04787-w

[50] Sridharan N, Gussev MN, Field KG (2019) Performance of a ferritic/martensitic steel for nuclear reactor applications fabricated using additive manufacturing. J Nucl Mater 521:45–55. https://doi.org/10.1016/j.jnucmat.2019.04.020

[51] Sun F, Meade ED, O'Dowd NP (2019) Strain gradient crystal plasticity modelling of size effects in a hierarchical martensitic steel using the Voronoi tessellation method. Int J Plast 119:215–229. https://doi.org/10.1016/j.ijplas.2019.03.009

[52] Sun F, Meade ED, O'Dowd NP (2018) Microscale modelling of the deformation of a martensitic steel using the Voronoi tessellation method. J Mech Phys Solids 113:35–55. https://doi.org/10.1016/j.jmps.2018.01.009

[53] Vaid A, Guénolé J, Prakash A, Korte-Kerzel S, Bitzek E (2019) Atomistic simulations of basal dislocations in Mg interacting with Mg17Al12 precipitates. Materialia 7:100355. https://doi.org/10.1016/J.MTLA.2019.100355

[54] Yamashita T, Onzawa T (1980) Martensites in austenitic stainless steel welded explosively. J Electron Microsc (Tokyo) 29:32–37. https://doi.org/10.1093/oxfordjournals.jmicro.a050205

[55] Zbib HM, Diaz de la Rubia T (2002) A multiscale model of plasticity. Int J Plast 18:1133–1163. https://doi.org/10.1016/S0749-6419(01)00044-4

[56] Zhang X, Lu S, Zhang B, Tian X, Kan Q, Kang G (2021) Dislocation–grain boundary interaction-based discrete dislocation dynamics modeling and its application to bicrystals with different misorientations. Acta Mater 202:88–98. https://doi.org/10.1016/j.actamat.2020.10.052

[57] Zhao J, Jiang Z (2018) Thermomechanical processing of advanced high strength steels. Prog Mater Sci 94:174–242. https://doi.org/10.1016/J.PMATSCI.2018.01.006

[58] Zhou X, Liu C, Yu L, Liu Y, Li H (2015) Phase transformation behavior and microstructural control of high-Cr martensitic/ferritic heat-resistant steels for power and nuclear plants: a review. J Mater Sci Technol 31:235–242. https://doi.org/10.1016/j.jmst.2014.12.001